



Cite this: DOI: 10.1039/c9sm02237f

Mechanically programmed 2D and 3D liquid crystal elastomers at macro- and microscale via two-step photocrosslinking†

Jieun Lee,^a Yuanhang Guo,^a Yu-Jin Choi,^b Soonho Jung,^{cd} Daehee Seol,^{cd} Subi Choi,^{id a} Jae-Hyuk Kim,^e Yunseok Kim,^{id cd} Kwang-Un Jeong^{id *b} and Suk-kyun Ahn^{id *a}

Liquid crystal elastomers (LCEs) are a unique class of active materials with the largest known reversible shape transformation in the solid state. The shape change of LCEs is directed by programming their molecular orientation, and therefore, several strategies to control LC alignment have been developed. Although mechanical alignment coupled with a two-step crosslinking is commonly adopted for uniaxially-aligned monodomain LCE synthesis, the fabrication of 3D-shaped LCEs at the macro- and microscale has been rarely accomplished. Here, we report a facile processing method for fabricating 2D and 3D-shaped LCEs at the macro- and microscales at room temperature by mechanically programming (i.e., stretching, pressing, embossing and UV-imprinting) the polydomain LCE, and subsequent photocrosslinking. The programmed LCEs exhibited a reversible shape change when exposed to thermal and chemical stimuli. Besides the programmed shape changes, the actuation strain can also be preprogrammed by adjusting the extent of elongation of a polydomain LCE. Furthermore, the LCE micropillar arrays prepared by UV-imprinting displayed a substantial change in pillar height in a reversible manner during thermal actuation. Our convenient method for fabricating reversible 2D and 3D-shaped LCEs from commercially available materials may expedite the potential applications of LCEs in actuators, soft robots, smart coatings, tunable optics and medicine.

Received 11th November 2019,
Accepted 9th February 2020

DOI: 10.1039/c9sm02237f

rsc.li/soft-matter-journal

Introduction

Shape programmable materials have attracted significant interest for applications in sensors, actuators and robotics owing to their tunable shape, structure, and properties in response to external stimuli.^{1–6} Various types of shape programmable materials have been investigated including hydrogels,^{7–10} shape memory polymers (SMPs),^{11–14} and liquid crystal elastomers (LCEs)^{15–20} and their composites.^{21–23} Among them, LCEs have received a keen attention because their solid-state shapes can be changed in a reversible and programmable manner by the

application of external stimuli, which can regulate the order parameter.¹⁵

Molecular alignment of the LCEs is the key to enabling the reversible and programmable shape transformation at both the macro- and microscale levels. Several strategies for controlling the LC director have been developed including the alignment induced by surface treatment, magnetic field and mechanical stretching, with each strategy having its own benefits and limitations.^{16,24} For example, surface treatment achieved through processes such as rubbing and photoalignment offers a spatial and hierarchical control of the director profile which can bring about complex 3D shapes (e.g., origami-inspired shapes and topological defects) under external stimuli.^{25–31} However, this method is typically limited by thin films (<100 μm) due to the decay of the alignment away from the surface.²⁴ Magnetic alignment based on permanent or electromagnets is particularly useful for obtaining microscale actuators and can be easily integrated with other processing methods, such as soft lithography.^{32–35} However, this technique is usually used to generate uniaxial alignment, while sophisticated magnet set-ups are required to obtain LCEs having complex director profiles.^{36,37} Recently, direct ink writing (DIW)-based additive manufacturing has also been demonstrated for shear-induced LC alignment

^a Department of Polymer Science and Engineering, Pusan National University, Busan, 46241, Korea. E-mail: skahn@pusan.ac.kr

^b Department of Polymer-Nano Science and Technology & Department of BIN Convergence Technology, Jeonbuk National University, Jeonju, 54896, Korea. E-mail: kujeong@jbnu.ac.kr

^c School of Advanced Materials and Engineering, Sungkyunkwan University (SKKU), Suwon, Gyeonggi-do, 16419, Korea

^d Research Center for Advanced Materials Technology, Sungkyunkwan University (SKKU), 2066 Seobu-ro, Jangsan-gu, Suwon, Gyeonggi-do, 16419, Korea

^e Department of Chemical and Environmental Engineering, Pusan National University, Busan, 46241, Korea

† Electronic supplementary information (ESI) available. See DOI: 10.1039/c9sm02237f

during extrusion, producing the 3D-shaped LCEs that can switch between two non-planar shapes.^{38–42}

Historically, mechanical alignment was first developed by Finkelmann *et al.* to prepare uniaxially aligned monodomain LCEs.⁴³ For this method, a two-step crosslinking process was employed, where a mixture of polyhydrosiloxane, vinyl-terminated mesogens, and crosslinkers first underwent gelation (partial crosslinking) inside a Teflon-coated cell *via* the hydrosilylation reaction, followed by second complete crosslinking under an external load to achieve uniaxial alignment. The two-step crosslinking method has been widely exploited to prepare side-chain,^{44,45} main-chain,^{46,47} photochromic,^{48–50} dye-doped LCEs,⁵¹ and LCE composites.^{52–54} Instead of the hydrosilylation reaction, Yakacki *et al.* recently explored a two-stage thiol-acrylate Michael addition and photopolymerization, which enabled a convenient route to prepare the monodomain main-chain LCEs.^{55,56} Based on this chemistry, a method to arbitrarily program curvatures in LCEs (i) by inhomogeneous stretching of polydomain LCE,⁵⁷ (ii) by curling a stretched monodomain LCE,⁵⁸ or (iii) by deforming the polydomain LCE *via* curling, stamping and embossing,⁵⁹ and subsequent crosslinking have been reported. Although mechanical alignment combined with a two-step crosslinking is commonly adopted mostly for uniaxially-aligned LCE synthesis, the fabrication of 3D-shaped LCEs at the macro- and microscale has been rarely accomplished.^{60,61}

In this work, we report a facile processing method for fabricating 2D and 3D-shaped LCEs at the macro- and microscale by mechanical alignment at room temperature. The 3D shape programmed main-chain LCEs were synthesized by melt processing using commercially available monomers through a two-step photocrosslinking process. First, diacrylate functionalized nematic monomer underwent chain extension by reacting with *n*-butyl amine through an aza-Michael addition reaction to obtain LC oligomers. Afterward, the LC oligomers were partially cured by UV crosslinking, generating polydomain LCEs which were then mechanically programmed *via* stretching, pressing, and embossing at room temperature. Lastly, the alignment in the LCE was locked by additional and complete UV crosslinking, resulting in mechanically programmed LCEs. 2D or 3D reversible actuations of the LCEs were successfully demonstrated when exposed to heat or solvent. Interestingly, the actuation strain of the LCEs can be preprogrammed by simply adjusting the extent of elongation of the polydomain LCEs without changing the formulation during the LCE synthesis. We further created thermally-responsive LCE micropillar arrays by UV-imprinting that showed considerable contraction and expansion of pillar height during heating and cooling, respectively. Our convenient method for fabricating 3D shape programmable LCEs can be easily extended to the development of macro- and microscale actuators, and may facilitate the potential applications of LCEs including soft robots, smart surfaces, tissue engineering substrates, tunable optics and haptic devices.

Experimental

Materials

1,4-Bis-[4-(3-acryloyloxyhexyloxy)benzoyloxy]-2-methylbenzene (RM257) was purchased from Synthon Chemical, and *n*-butylamine

(*n*-BA) was purchased from Sigma-Aldrich. Irgacure-369 (I-369) was donated by BASF corporation.

Preparation of liquid crystal cells

Glass slides were wiped using acetone to remove stains and dust, and then sonicated with isopropanol. To generate hydrophilic surface, the glass slides were treated with air plasma for 10 min. Afterward, the glass slides were spin coated with Elvamide solution (0.125 wt% in methanol) and rubbed using a velvet cloth. The LC cells were made by assembling two rubbed glass slides separated by 100 μm spacers.

Preparation of shape programmed LC elastomers

Shape programmed LCEs were synthesized by aza-Michael addition-based step-growth polymerization and radical photocrosslinking. In a 6 mL vial, LC monomer, *n*-BA, and I-369 were added, where the molar ratio of LC monomer to *n*-BA was 1.1:1, and the amount of I-369 was 2.5 wt% of the total LC mixture. After thorough mixing with a heat gun and a vortex, the LC mixture was filled into an LC cell at 65 °C (nematic temperature). Then, the cell containing the LC mixture was placed in 65 °C oven for 21 h for oligomerization. We note that oligomerization can also be performed at isotropic temperature (e.g., 90 °C) which may help to reduce the reaction time.

The LC oligomer was first exposed to weak UV light (OmniCure LX405S, $\lambda = 365 \text{ nm}$, 1.5 mW cm^{-2}) for 6 s at 90 °C (isotropic temperature), which resulted in a partially cured polydomain LCE. We note that if the sample was prepared in an unrubbed glass cell, optical uniformity of the resulting polydomain LCE was not guaranteed as shown in Fig. S1 (ESI†). Next, the polydomain LCE was mechanically programmed into a desired shape and immediately exposed to high powered UV light (OmniCure S1500, $\lambda = 365 \text{ nm}$, 30 mW cm^{-2}) for 30 min at room temperature. The second photocrosslinking allowed shape fixing of the LCE, which resulted in a shape programmed LCE.

Methods and characterization

¹H NMR spectra was recorded on a 500 MHz Varian spectrophotometer using CDCl₃. Attenuated total reflectance Fourier transform infrared spectroscopy (ATR-FTIR) spectra were recorded on a Agilent technologies Cary 640 spectrometer. A background spectrum (64 scans at 4 cm^{-1} resolution) of a clean ATR crystal was used as the reference. A total of 64 scans were collected at a resolution of 4 cm^{-1} , and OPUS software was used to process the spectra. A polarizing optical microscope (POM, Nikon Eclipse LV100N POL) coupled to a heating stage (Linkam LTS420) using Touptview software was used to determine the alignment and phase transition temperature. Photographs of the LCEs were taken by a Canon EOS REBEL T3 camera (CANON MACRO LENS EF 100 mm, 1:2.8 USM). A laser scanning confocal microscope (Olympus OLS5000) coupled to a heating stage was used to characterize the thermal actuation of the LCE micropillar arrays. During this measurement, the cover of the heating plate was removed, and therefore, the temperature was calibrated using a thermocouple. The temperature dependent confocal microscope images were analyzed using a MATLAB-based home-made program.

Since the absolute height value can differ for each image, the height value was calibrated based on the reference point (see the Point 1 in Fig. 8e). The images with calibrated height values are represented in Fig. S11 (ESI[†]). Temperature dependent transmission measurement of the LCE film was performed by multipurpose spectrometer (Otsuka Electronics, MCPD-3000) equipped with a heating stage. Differential scanning calorimetry (DSC) was performed by the TA instruments Q20 calorimeter. A 4 mg sample was heated to 200 °C to remove any thermal history, cooled to −50 °C, and then re-heated to 200 °C at a rate of 10 °C min^{−1}. Thermogravimetric analysis (TGA) was performed by the TA instruments Q50. A 10 mg sample was heated to 800 °C at a rate of 10 °C min^{−1} under an argon atmosphere.

Mechanical and viscoelastic properties

The mechanical and viscoelastic properties of the LCE were characterized by a dynamic mechanical analyzer (DMA, TA instruments Q850) using a tension film clamp. In a stress-strain measurement, a sample ($L \times W \times T = 5.5 \times 3.6 \times 0.1$ mm) was equilibrated at 30 °C under a preload of 1 mN, and the force was increased at a rate of 0.2 N min^{−1}. The viscoelastic property of the LCE was investigated by heating the polydomain LCE ($L \times W \times T = 7.6 \times 3.2 \times 0.1$ mm) from −100 to 200 °C at a rate of 3 °C min^{−1} under a constant frequency of 1 Hz. The glass transition temperature (T_g) was determined by the maximum peak of the $\tan \delta$ curve.

Wide-angle X-ray diffraction

To estimate the molecular orientation in the LCE films, 2D wide-angle X-ray diffraction (WAXD) patterns were obtained by exposing X-ray (an 18 kW rotating anode X-ray generator) on a Rigaku X-ray imaging system for 15 min. The background scattering was subtracted from the sample scans to obtain a suitable quality X-ray pattern. The position and width of the diffraction peaks were calibrated with silicon powder ($2\theta = 28.466^\circ$). To quantify the degree of orientation in the LCE films, azimuthal angle was scanned from 0° to 180° in the high 2θ -angle region ($2\theta = 15^\circ$ – 24°). Order parameter (S) was calculated by $(180^\circ - H^\circ) \times 100/180^\circ$. Here H° represents the half-width of the intensity distribution on the Debye diffracted arc.

Gel fraction

Crosslinked samples were immersed in chloroform for 48 h to extract the uncrosslinked part of the LCEs. Then, the samples were dried in a vacuum oven for 24 h at room temperature. The gel fraction (G) was calculated by

$$G(\%) = \frac{m_f}{m_i} \times 100\%$$

where m_i is the initial mass of the LCE before extraction, and m_f is the final dried mass of the LCE after extraction.

Fabrication of micropatterned acryl resin

The micropatterned master mold and the polydimethylsiloxane (PDMS) replica mold were first fabricated by a previously described process.⁶² The PDMS replica mold was used as a stamp mold to make the micropatterned acryl resin. The PDMS

replica mold was pressed into *ca.* 60 μ L of UV-curable acrylic oligomer droplet (MINS 311RM, Minuta Tech. Korea) on a PET film, exposed to UV ($\lambda = 365$ nm) for 1 h at room temperature and then carefully removed. The resulting micropattern-transferred acryl resin was washed with water several times and stored for further use.

Results and discussion

An LCE was synthesized by following a previously reported protocol^{28,63,64} that is described in Fig. 1a. Briefly, an LC monomer (RM257) underwent chain extension by reacting with *n*-butylamine *via* aza-Michael addition-based step growth polymerization, which resulted in a diacrylate-functionalized poly(β -amino ester) type LC oligomer. A nematic phase was observed for the LC oligomer as evidenced by the Schlieren texture under POM (Fig. S2, ESI[†]). The nematic-isotropic temperature (T_{ni}) of the LC oligomer determined by POM during cooling from the isotropic phase was 72 ± 2 °C. The diacrylate end groups in the LC oligomer were then covalently linked by UV-induced radical polymerization, producing an LCE. The reactions were conducted inside an LC cell to obtain an LCE film with uniform thickness (100 μ m). The degree of polymerization and number average molecular weight of LC oligomer determined by ¹H NMR end group analysis were 6.6 and 5000 g mol^{−1}, respectively (Fig. S3, ESI[†]).

To prepare mechanically programmed LCEs, the photocrosslinking procedure was performed in a two-step process, as illustrated in Fig. 1b. First, the LC oligomer in the LC cell was only partially crosslinked by exposure to weak UV light (1.5 mW cm^{−2}) for 6 s at 90 °C (isotropic temperature). After partial crosslinking, the initially transparent sample became opaque, suggesting the formation of polydomain LCE.^{43,55,63} Then, the polydomain LCE was separated from the cell and mechanically programmed (*i.e.*, stretching or pressing with a mold) to obtain desired shapes. Subsequently, the deformed shapes of the polydomain LCE were successfully fixed by stronger UV crosslinking (30 mW cm^{−2}) for 30 min at room temperature, resulting in mechanically programmed LCEs.

In our protocol, to prepare mechanically programmed LCEs, finding conditions under which a polydomain LCE can be obtained after the first photocrosslinking process is critical. On one hand, if the degree of the first crosslinking is too high (*e.g.*, resulting from too long UV exposure or too high crosslinking temperature), the mechanical deformation of the polydomain LCE as well as subsequent shape fixing process becomes limited. Also, if the crosslinking temperature is too high such as 100 °C, the isotropic networks can be trapped due to high radical reactivity which may produce an optically and structurally less-uniform polydomain LCE. On the other hand, if the degree of crosslinking is insufficient (*e.g.*, resulting from too short UV exposure or too low crosslinking temperature such as 80 °C), the mechanical stability of the polydomain LCE cannot be guaranteed (Fig. S4, ESI[†]). Therefore, we attempted to optimize the first photocrosslinking condition by monitoring gel fraction values of polydomain LCEs cured at various UV exposure times

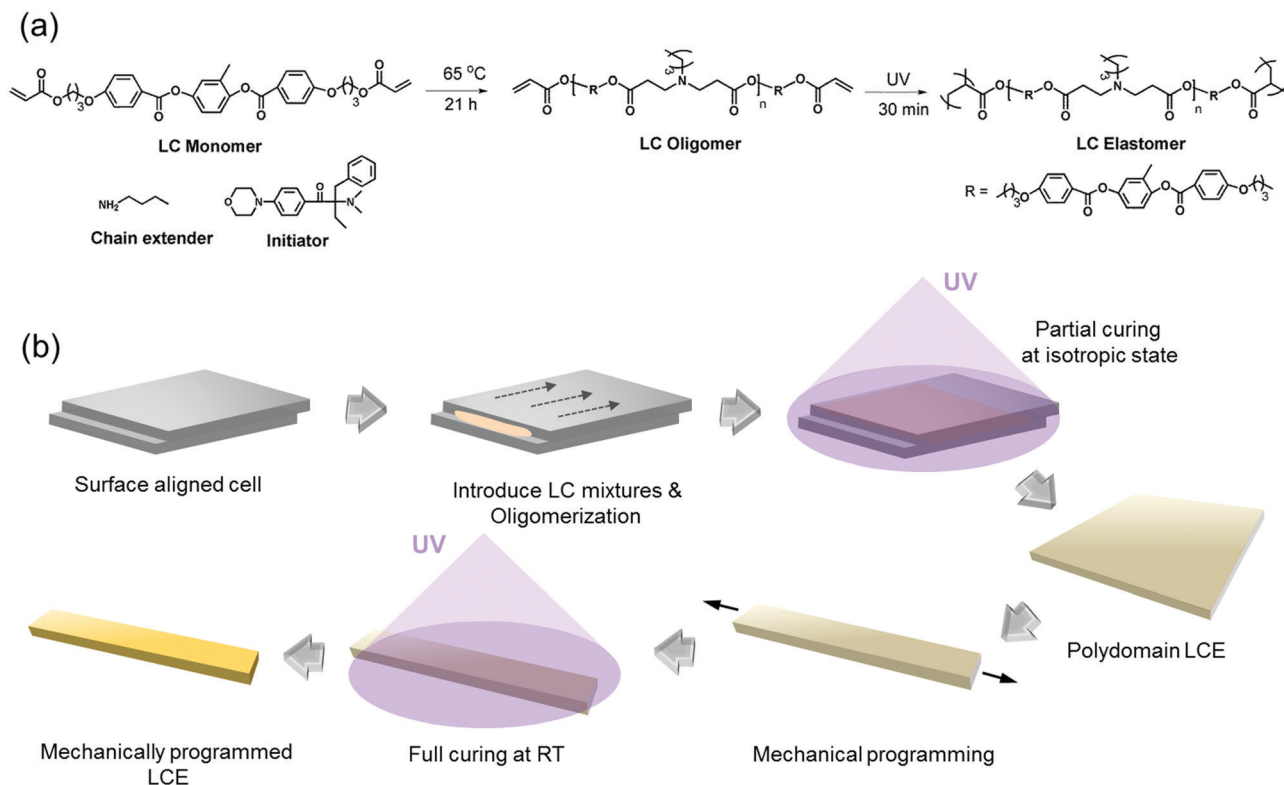


Fig. 1 (a) Reaction scheme for LCE synthesis. (b) Procedure for preparing a mechanically programmed LCE by the two-step photocrosslinking method.

while keeping other conditions the same ($\lambda = 365$ nm, 1.5 mW cm^{-2} , and 90°C).

The gel fraction gradually increases with increasing UV exposure time, which indicates the formation of denser chain networks (Fig. 2, Fig. S5 and Table S1, ESI†). It was found that a too short photocrosslinking (< 6 s) could not generate enough networks in the polydomain LCE, and reliable values of the gel fraction were not determined. We note that the transparency of the sample gradually increases with increasing photocrosslinking time probably because

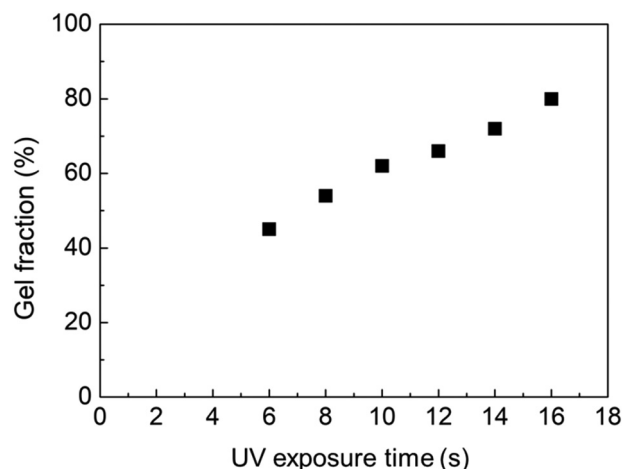


Fig. 2 Change in gel fraction values after partial photocrosslinking with different UV exposure times at 90°C .

of the arrestment of isotropic orientation. More importantly, longer photocrosslinking (> 10 s) generates very high gel fraction values (*i.e.*, high degree of crosslinking), and the shape fixing of a mechanically deformed LCE by the second photocrosslinking becomes less efficient. Based on these results, the first photocrosslinking period was set as 6 s at 90°C in our experiments, which resulted in the generation of a mechanically robust polydomain LCE along with a sufficient amount of unreacted acrylate groups for efficient shape fixing of the mechanically programmed LCE in the second photocrosslinking process.

To further understand the extent of acrylate reaction during photocrosslinking, FT-IR spectra of polydomain LCEs at various UV exposure times were examined, especially by monitoring the acrylate peak ($\text{C}=\text{C}$) at 810 cm^{-1} , which decreased with increasing UV-curing time (Fig. S6a and b, ESI†). The extent of reaction determined by the method reported by Sung *et al.*⁶⁵ shows a sharp increase to 54% at 4 s, and thereafter a gradual increase up to 74% until 10 s (Fig. S6c, ESI†). We note that the values between gel fraction and the extent of reaction can show a difference, although both results show a similar tendency. This is because gel fraction was determined with samples after extracting uncured parts, while the extent of reaction from FT-IR was determined with samples without any treatment. The gel fraction value of the programmed LCE after second intensive crosslinking was approximately 92%.

The thermal and mechanical properties of the polydomain LCE are important for determining the shape programming and thermal actuation conditions of mechanically programmed LCEs. For these analyses, a fully photocrosslinked polydomain

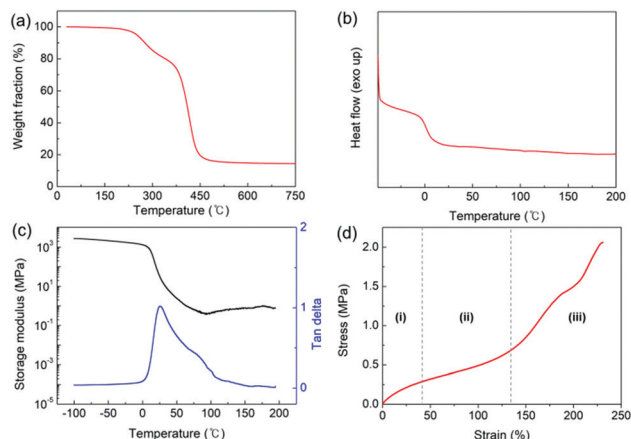


Fig. 3 (a) TGA curve of the fully crosslinked polydomain LCE. (b) DSC second heating curve of the fully crosslinked polydomain LCE. (c) Viscoelastic property of the fully crosslinked polydomain LCE. (d) Stress–strain curve of the partially crosslinked polydomain LCE. Three regions are identified: (i) the polydomain, (ii) the polydomain-monodomain transition, and (iii) the monodomain region.

LCE was used for TGA, DSC, and viscoelastic measurements, while a partially crosslinked polydomain LCE was used for the stress–strain measurement. The polydomain LCE decomposes at 249 °C, as determined by TGA, at which a 5% weight loss occurs (Fig. 3a). We note that the two-step degradation process is associated with alkyl side chain originating from *n*-butyl amine (for first decomposition) and with main-chain LCE network (for second decomposition).⁶⁴ The glass transition temperature (T_g) determined by the DSC measurement during the second heating process was -1 °C (Fig. 3b), while the T_g determined by the DMA measurement with a maximum peak of the $\tan \delta$ curve was 25 °C (Fig. 3c). **The higher T_g observed in DMA is caused by a larger sample size, which causes slower heat transfer to the sample, and by the difference in measurement conditions between DSC (static condition) and DMA (dynamic oscillation condition).**

The T_{ni} of the polydomain LCE was not clearly detected in both DSC and DMA, but a slight shoulder appearing in the $\tan \delta$ curve at around 80 °C suggests T_{ni} at this temperature. Indeed, a sharp shape change occurs around this temperature when heating the uniaxially aligned monodomain LCE and will be discussed later. When heated above T_{ni} , the rubbery plateau was clearly observed, indicating the efficient formation of a network structure by photocrosslinking. The crosslink density of the polydomain LCE was calculated by the following equation:⁶⁶

$$\nu_e = \frac{E'}{3RT}$$

where ν_e is the crosslink density, E' is storage modulus at 150 °C (*i.e.*, at rubbery plateau), R is the gas constant, and T is the temperature in K. The crosslink density of the fully cured polydomain LCE was $7.3 \times 10^{-5} \text{ mol cm}^{-3}$.

The stress–strain relationship of a partially crosslinked polydomain LCE (*i.e.*, after first and weak photocrosslinking) was investigated by a tensile test conducted at 30 °C (Fig. 3d).

The polydomain LCE exhibits classical soft elastic behavior upon tensile loading, which consists of three characteristic regions: (i) the polydomain, (ii) the polydomain-monodomain transition (due to orientation of the director to the loading direction), and (iii) the monodomain.^{58,67} Due to loosely cross-linked networks, the polydomain LCE can be elongated by 230%, which suggests that LCEs can be mechanically programmed with a large deformation.

The polydomain LCE obtained after partial photocrosslinking can be mechanically programmed into various 2D or 3D shapes. First, we investigated the characteristics of a simple monodomain LCE, which was prepared by uniaxially stretching a polydomain LCE by 200%, relaxing until 75% at room temperature, and then fixing the stretched shape through intensive photocrosslinking. The homogeneous alignment of the sample was confirmed by rotating the director between cross polarizers (Fig. 4a). The 2D-WAXD patterns and their corresponding azimuthal scans of the polydomain LCE and the uniaxially stretched monodomain LCE are shown in Fig. 4b. The intensive diffraction arc on the equator was observed for the uniaxially stretched LCE, while a uniform ring was detected for the polydomain LCE. The order parameter (S) of the monodomain LCE determined by the azimuthal scan was 0.84. The high order parameter of the monodomain LCE suggests a strong orientation of the director was induced by mechanical alignment, which was successfully locked in the LCE by photocrosslinking.

A reversible thermal actuation of the uniaxially aligned monodomain LCE was further investigated by monitoring dimensional changes in the sample during heating and cooling under POM, and the results are shown in Fig. 4c. The monodomain LCE exhibits a considerable contraction ($\epsilon = 38\%$) in length (*i.e.*, parallel to the director) on heating, and the most rapid contraction is observed at 75 °C, as indicated by the peak of the first derivative of the length with respect to temperature. Under cooling to room temperature, the monodomain LCE becomes spontaneously

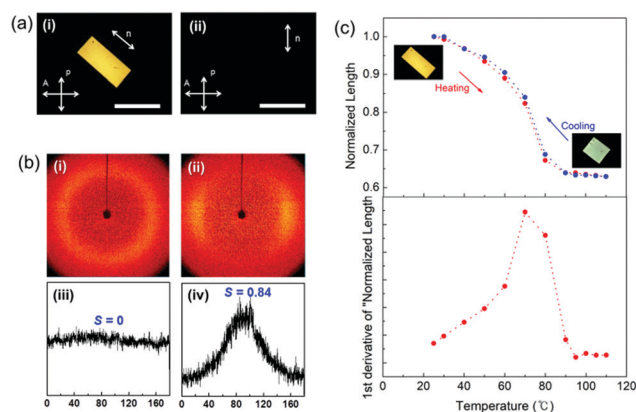


Fig. 4 (a) POM images of a uniaxially aligned LCE positioned at (i) 45° and (ii) 0° with respect to the cross polarizers. Scale bars represent 500 μm . (b) 2D-WAXD patterns and corresponding azimuthal scans of 2θ angle between 15° and 24° in 2D-WAXD for (i and iii) the polydomain LCE and (ii and iv) the uniaxially aligned LCE at room temperature. (c) Reversible thermal actuation of the uniaxially aligned LCE: inset shows the POM images of the sample taken at 25 and 110 °C.

elongated and recovers to its initial length, demonstrating excellent reversibility of thermal actuation without hysteresis.

While the surface alignment is beneficial for spatial and hierarchical control of the director profile,^{27,28,67–71} and the magnetic alignment is useful for preparing microactuators,^{32–35} mechanical programming can be more versatile for shape programming LCEs. For example, various shapes of 1D, 2D, and 3D LCEs can be prepared, such as fibers, films, 3D objects and patterns by tensile, shear and compression forces.^{58,59,72–77}

In addition, the degree of LC alignment can be precisely controlled by adjusting the force applied.

By taking advantage of mechanical programming, we first attempted to prepare mechanically programmed LCEs with different degrees of LC alignment. To understand the relation between different degrees of mechanical alignment and actuation behavior, four monodomain LCEs were prepared by uniaxially stretching the initial length (12 mm) of polydomain LCE films by 67, 100, 150, and 200%, which was followed by photocrosslinking to lock the alignment. It should be noted that the stretched samples were instantly relaxed to a certain degree due to the elastic recovery of partially crosslinked networks within the polydomain LCEs. As a result, the intensive photocrosslinking was performed on the stretched samples after the relaxation process was completed. If the second photocrosslinking was performed before the relaxation completed, the actuation was not fully reversible (especially for the first cycle). The final monodomain LCEs were elongated by 8, 42, 58, and 75% with respect to the initial length. The dimensional changes for each sample during mechanical programming are described in Fig. 5a, Fig. S7a (ESI[†]), and Table 1.

Interestingly, four monodomain LCEs exhibit different extents of thermal contraction depending on the initial degree of stretching, while the actuation temperature remains similar for all samples (Fig. 5b, Fig. S7c, ESI[†] and Table 1). It was found that if the degree of stretching is too small (sample 1), thermal contraction is not clear, implying the presence of threshold strain to activate noticeable actuation. The negligible actuation in sample 1 is also associated with insufficient alignment of the director evidenced by photographs taken between cross polarizers (Fig. S7b, ESI[†]). In fact, the stress-strain curve of the partially crosslinked polydomain LCE (Fig. 3d) suggests the polydomain-monodomain transition (resulting from the reorientation of LC director) starts to appear above 50% strain. Therefore, the polydomain LCE needs to be stretched well above the 50% strain to induce sufficient alignment of the LC director and to show a noticeable actuation. In contrast to sample 1, samples 2–4, which were initially stretched by more than 100% exhibit clear contraction during heating. In general, the higher the elongation, the larger the observed thermal actuation, which is probably due to stronger alignment. However, the difference in actuation strain between sample 3 and sample 4 is insignificant, which suggests comparable LC ordering in these samples (Fig. 5b). These results suggest that the thermal actuation strain of the monodomain LCE can be

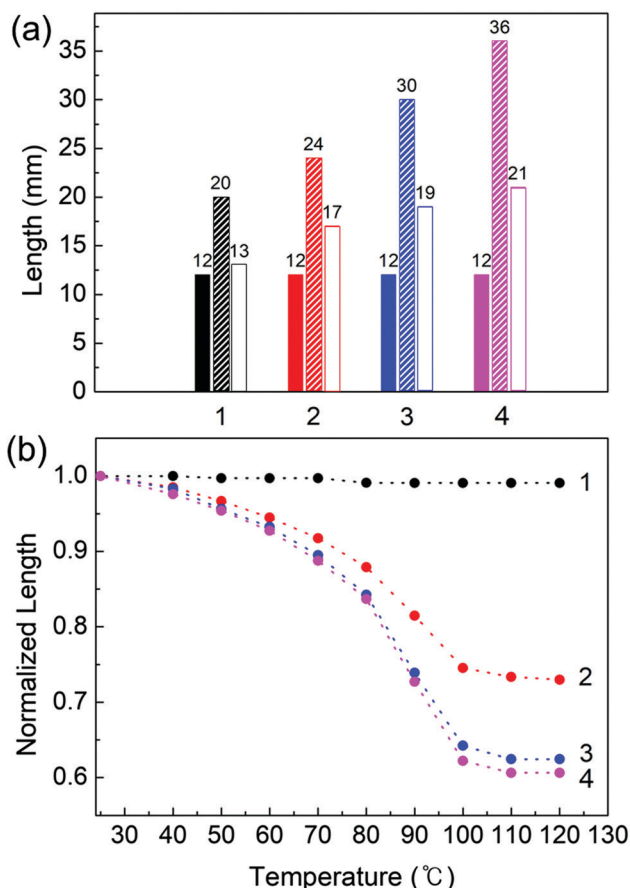


Fig. 5 (a) Length changes of uniaxially stretched LCEs programmed by different degrees of elongation; the filled rectangular bars (left) are initial sample lengths, partially filled rectangular bars (middle) are the sample lengths after stretching, and unfilled rectangular bars (right) are the sample lengths after instant relaxation. (b) Thermal actuation of uniaxially stretched LCEs, programmed by different degrees of elongation, monitored by POM.

Table 1 Summary of programming and actuation of uniaxially stretched monodomain LCEs programmed by different degrees of elongation

Sample	L_0 (mm)	After uniaxially stretched		After relaxed, crosslinked		Actuation ε^b (%)	Actuation ε^c (%)
		L (mm)	ε^a (%)	L (mm)	ε^a (%)		
1	12	20	67	13	8	8	0.9
2	12	24	100	17	42	30	27
3	12	30	150	19	58	37	37
4	12	36	200	21	75	43	39

^a Calculated by $[(\text{stretched length}) - (\text{initial length})]/(\text{initial length}) \times 100$. ^b Calculated by $[(\text{the length after photocrosslinked}) - (\text{the contracted length at } 120^\circ\text{C})]/(\text{the length after photocrosslinked}) \times 100$. ^c Determined by POM using a heating stage with the LCEs with small dimensions. Typical size of the sample was 1.35 mm (L) \times 0.34 mm (W) \times 0.081 mm (T).

mechanically preprogrammed and reveal a strong dependence on the extent of initial stretching of the polydomain LCE.

In addition to the uniaxially aligned 2D LCE film, we also prepared various LCEs having 3D shapes and demonstrated their reversible shape changes as shown in Fig. 6. For these 3D-shaped LCEs, the partially crosslinked polydomain LCEs were mechanically programmed in various manners: (i) by stretching in the biaxial direction (for a biaxially stretched LCE), (ii) by adhering both ends of a uniaxially stretched LCE while winding a roller (for a ring-shaped LCE), and (iii) by pressing with a cylindrical-shaped mold only at the center of the film (for a hat-shaped LCE). Afterward, the shapes of the deformed LCEs were effectively fixed by photocrosslinking for 30 min at room temperature. In particular, both opaque and transparent regions were observed for the hat-shaped LCE, which implies different orientations of LC directors were induced during pressing. Indeed, 2D-WAXD patterns show a strong ordering ($S = 0.78$) for the transparent region (*i.e.*, side of the hat) indicating the orientation of LC directors parallel to the pressing direction, whereas no orientations are observed for the rest of the opaque regions (*i.e.*, top and bottom of the hat) as shown in Fig. S8 (ESI[†]).

When heated above T_{ni} , the biaxially stretched LCE and the hat-shaped LCE transformed to their initial flat shapes (*i.e.*, the shapes prior to programming). The variation in the area of the biaxially-stretched LCE is about 6%, and the height change of the hat-shaped LCE is 1.8 mm. On the other hand, heating above T_{ni} causes a decrease in the diameter of the ring-shaped LCE from 4.9 to 3.7 mm, and thereby the area changes by 43%. Upon cooling to room temperature, all LCE samples return to their programmed shapes, demonstrating dynamic and reversible shape changes (Videos S1–S3, ESI[†]).

Successful preparation of the aligned LCE by pressing through a mold inspired us to employ various types of patterned molds to

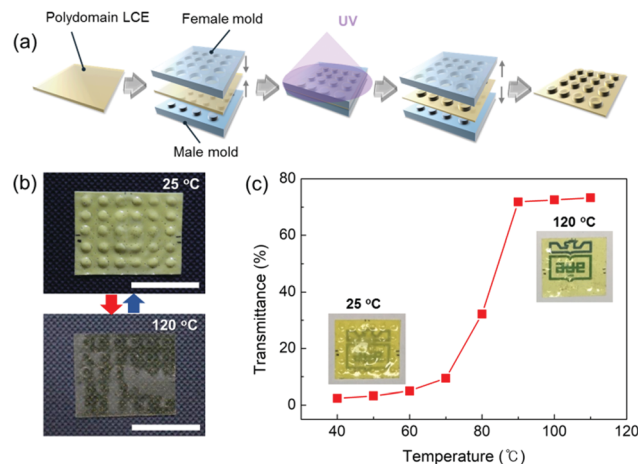


Fig. 7 (a) Illustration of a programmed LCE pattern by embossing using a male and a female mold. (b) Reversible shape change of the LCE pattern (6×5 array) during heating and cooling. Scale bars indicate 5 mm. (c) Change in transmittance as a function of temperature: the inset shows the photographs of the patterned LCE at 25 and 120 °C.

create responsive LCE surfaces *via* embossing and imprinting. For this purpose, the partially crosslinked polydomain LCE was compressed between millimeter size male and female molds made with acryl resin for 10 min at room temperature, followed by photocrosslinking for 30 min (Fig. 7a). Through this process, a patterned LCE surface at the macroscale with an embossed circular shape with a diameter and height of approximately 2.0 and 0.5 mm, respectively, was successfully prepared (Fig. 7b). Upon heating above T_{ni} , the protruding regions became flat, and the transparency increased significantly due to loss of LC ordering (Fig. 7b and Video S4, ESI[†]). More specifically, the transmittance of the patterned LCE increased from 2 to 73% with a rapid change at around 80 °C (Fig. 7c). The transmittance change profile with temperature shows a similar trend with the dimensional change profile during thermal actuation (Fig. 4c). When the LCE was cooled to room temperature, the programmed 3D surface patterns were recovered, and the sample became opaque.

The LC ordering can also be disrupted not only by thermal stimulus, but also by chemical stimulus (*e.g.*, by exposing the LCE to a good solvent).^{28,78–80} To demonstrate this potential, the patterned LCEs were exposed to THF vapor inside a chamber. After 20 min of exposure, the LCE becomes flat and optically transparent (Fig. S9, ESI[†]), which was similar to the result obtained by heating the LCE above T_{ni} . Such changes are due to the penetration of solvent molecules into chain networks, which destroys the LC order. The chemoresponsive behavior of our LCEs can be exploited to develop a volatile organic compounds (VOC) sensor.

The fabrication of LCE micropillar arrays *via* UV imprinting and its reversible actuation are further demonstrated in Fig. 8. In the fabrication, a partially crosslinked polydomain LCE film (thickness = 100 μm) was compressed by a micropatterned acryl resin mold containing arrays of cylindrical holes from the top with 0.2 Ton for 10 min at room temperature. The height and the diameter of the holes in the acryl resin mold were 91 and

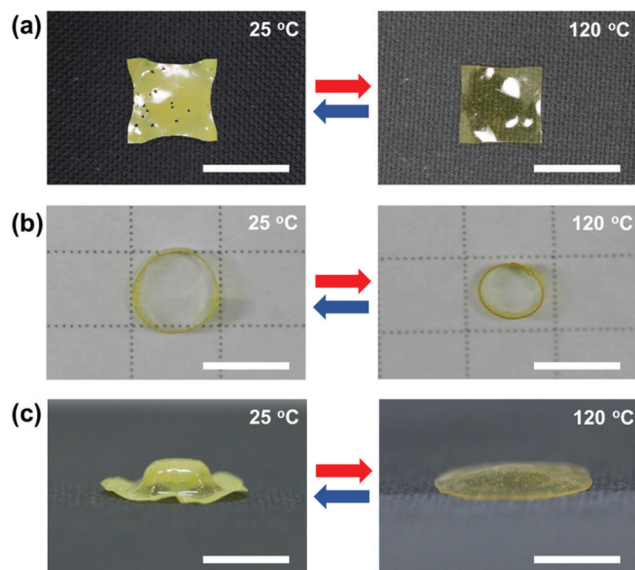


Fig. 6 Reversible shape changes of 3D-shaped LCEs during heating and cooling. (a) A biaxially-stretched LCE, (b) a ring-shaped LCE, and (c) a hat-shaped LCE. Scale bars indicate 5 mm.

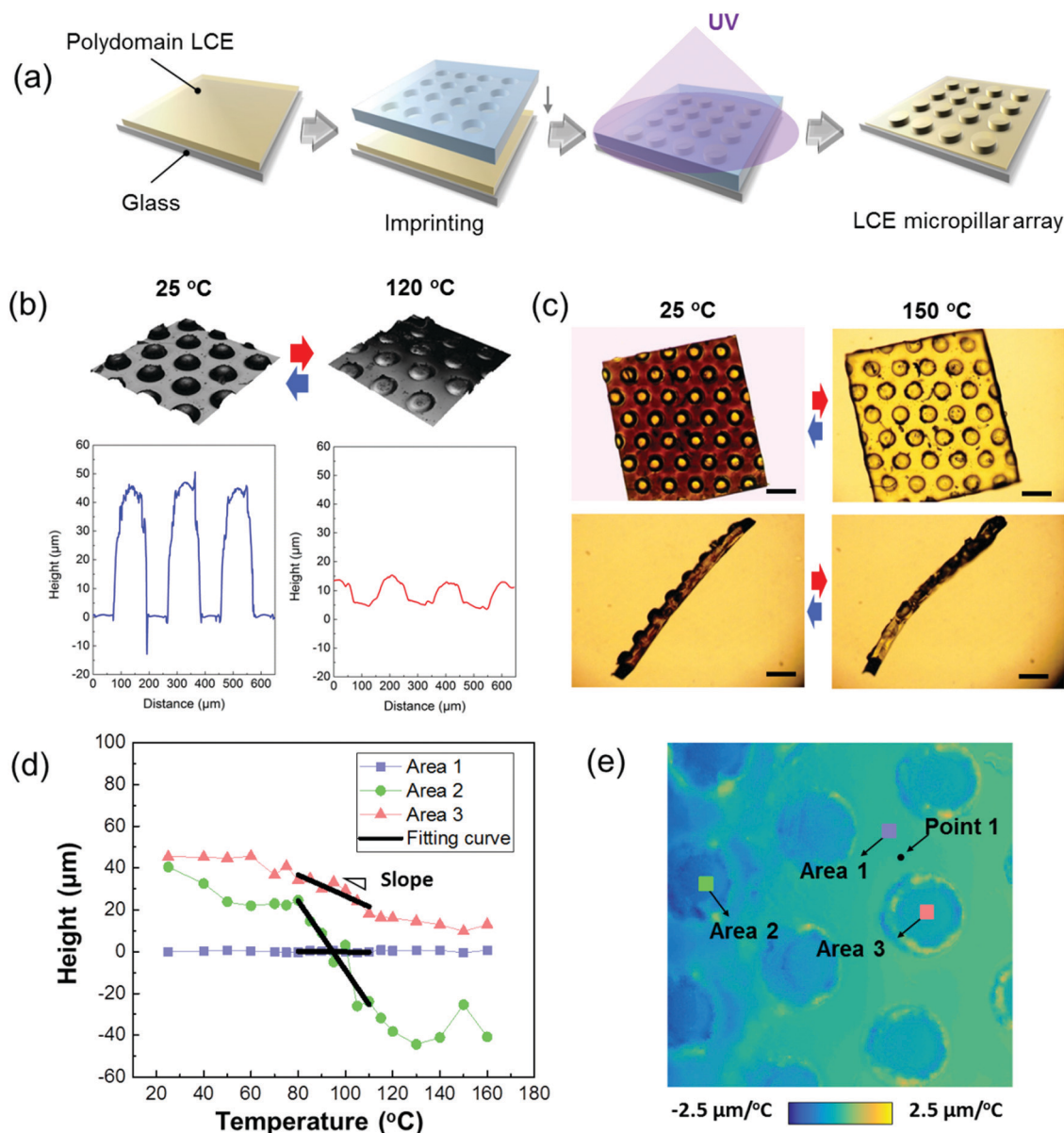


Fig. 8 (a) Fabrication of the LCE micropillar arrays via UV imprinting. (b) Reversible shape change of the LCE micropillar arrays. 3D topography images and height profiles of LCE micropillars at 25 and 120 °C recorded by a laser scanning confocal microscope. The height of the pillars decreases from 46 to 8 μm . (c) Optical microscope images (top-view and side-view) of the LCE micropillar arrays at 25 and 150 °C. Scale bars represent 100 μm . (d) Height change profiles of LCE micropillars extracted from the different points indicated in (e) as a function of temperature. (e) Spatial map of the height changing slope extracted by linear fitting in range from 80 to 110 °C. The area 1, 2 and 3 were averaged over the points of a 50×50 grid, i.e., 2500 points. The linear fitting was performed using the least square method.

96 μm , respectively (Fig. S10, ESI†). Subsequently, the LCE compressed by the mold was exposed to UV light for 30 min at room temperature in order to fix the deformed structure. Lastly, arrays replicating the acryl resin mold were obtained.

The pillars of the micropillar arrays show an average height of 46 ± 2 μm and average diameter of 118 ± 2 μm , as characterized by a laser scanning confocal microscope shown in Fig. 8b. The shorter height of the pillar compared to the height of the mold may be due to a certain degree of elastic recovery of partially crosslinked networks as well as incomplete mesogens filling the cylindrical holes.

When the LCE micropillar arrays were heated to 120 °C, the height of the pillars contracted to 8 ± 1 μm , while the diameter of the pillars expanded only slightly (Fig. 8b). The substantial contraction of pillar height indicates the mesogens were aligned along the longitudinal direction of the pillars, which was generated by shear force during imprinting.⁶⁰ The alignment direction of the mesogens in the micropillars can be further supported by the result of 2D-WAXD patterns of the hat-shaped LCE prepared by embossing (Fig. S8, ESI†). When the LCE micropillar arrays were cooled down to room temperature, the initial height of the pillars was recovered. The reversible actuation

of LCE micropillars was further examined by monitoring their shape changes using an optical microscope during temperature variation. During heating, the focus of the top-view image was continuously blurred, implying the occurrence of variation in pillar structure. At the same time, the whole LCE film became transparent at temperature above T_{ni} (Fig. 8c). Additionally, the side-view of the LCE micropillars shows a clear shrinkage of pillar height when the LCE is heated above T_{ni} (Fig. 8c). Apparently, the results of confocal and optical microscope analyses demonstrate the reversible height change of the LCE micropillar arrays.

The characteristics of thermal actuation in the bulk and microstructures may be different because of numerous interfaces presented in the microstructures. Therefore, we further investigated the change in height profiles as a function of temperature (Fig. 8d and e). The heights of the LCE micropillars decrease with increasing temperature. Their height starts to significantly decrease around 80 °C and then, saturate around 120–130 °C (areas 2 and 3 in Fig. 8d). We further examined the relationship between height variation of micropillars and temperature by extracting the linear slope *via* linear fitting ($ax + b$) in the temperature range from 80 to 110 °C (Fig. 8e). The extracted slope values range from around -1.70 to $-0.50 \mu\text{m } ^\circ\text{C}^{-1}$, and provide insight on how LCE micropillar structures vary depending on the temperature. The spatial map of the slope shown in Fig. 8e reveals that the height changing slope is varied at different locations: the inner region of the LCE micropillar shows an abrupt decrease in height, while the height of both matrix and the interface are relatively unchanged. We note that the left part of the slope image (area 2) is much steeper compared to the right part of the slope image (area 3), which may be related to the long-range shape change (or fluctuation) of the sample during heating.

The preparation of LCE micropillar arrays and their thermally-induced shape changing behaviors have been reported previously using magnetic alignment.^{32–34,81} However, the employment of magnetic alignment is typically challenging for scaling up and the fabrication for complex-shaped microstructures. In addition, the LC monomers in these systems were synthesized by multiple organic reactions. Recently, the Cai research group developed self-healable LCE micropillar arrays with thermal imprinting performed at 180 °C for 3 h, but only with a marginal height change (from 42.5 to 35 μm). By contrast, our fabrication strategy for LCE micropillar arrays is more convenient because the LCE can be synthesized using commercially available monomers, and the UV-imprinting can be performed at room temperature within 40 min (*i.e.*, 10 min for compression and 30 min for photocrosslinking). Also, the large height change (from 46 to 8 μm) of our LCE micropillar arrays in a reversible way can prove advantageous when the arrays are used in various types of responsive microstructures that are expected to have tunable wettability,^{82–84} friction^{85,86} and adhesion.^{32,87}

Conclusions

In summary, 2D and 3D-shaped LCEs at the macro- and micro-scale were prepared by mechanical programming (*i.e.*, stretching,

pressing, embossing, and UV-imprinting) of unoriented polydomain LCEs and subsequent photocrosslinking. The entire process used to prepare the programmed LCEs was carried out in the absence of a solvent, and the mechanical programming can be conveniently performed at ambient temperature. The programmed LCEs exhibited reversible actuation by heating and cooling, and by exposure to a solvent. In addition to the shape programming, the actuation strain can be also preprogrammed by simply adjusting the extent of elongation of the polydomain LCE without changing the formulation during the LCE synthesis. The LCE micropillar arrays prepared by UV-imprinting exhibited a substantial change in pillar height in a reversible manner when exposed to heat. The careful image analyses revealed that the inner regions of the LCE micropillar show more abrupt height changes than the interface between the micropillar and matrix. Our convenient method for obtaining shape programmable LCEs may expedite the potential applications of the LCEs in actuators, soft robots, smart coatings, optics, and medicine.

Conflicts of interest

The authors declare no competing financial interests.

Acknowledgements

This work was supported by Basic Science Research Program through the National Research Foundation of Korea (NRF) funded by the Ministry of Education (2019R1C1C1006048, 2019R1A6A1A03033215 and 2019M3D1A2103918). J. Lee and Y. Guo acknowledge BK21PLUS Program for partial financial support, and Hyeong-Ho Yoon for helpful discussion. The authors are grateful to Yeongyu Choi and Taehoon Yoon for helping temperature-dependent transmittance measurement.

References

- 1 H. Ko and A. Javey, *Acc. Chem. Res.*, 2017, **50**, 691–702.
- 2 Y. Liu, J. Genzer and M. D. Dickey, *Prog. Polym. Sci.*, 2016, **52**, 79–106.
- 3 T. van Manen, S. Janbaz and A. A. Zadpoor, *Mater. Today*, 2017, **21**, 144–163.
- 4 J. Zhou and S. S. Sheiko, *J. Polym. Sci., Part B: Polym. Phys.*, 2016, **54**, 1365–1380.
- 5 X. Fan, J. Y. Chung, Y. X. Lim, Z. Li and X. J. Loh, *ACS Appl. Mater. Interfaces*, 2016, **8**, 33351–33370.
- 6 G. Stoychev, A. Kirillova and L. Ionov, *Adv. Opt. Mater.*, 2019, 1900067.
- 7 J. Kim, J. A. Hanna, M. Byun, C. D. Santangelo and R. C. Hayward, *Science*, 2012, **335**, 1201–1205.
- 8 O. Erol, A. Pantula, W. Liu and D. H. Gracias, *Adv. Mater. Technol.*, 2019, **4**, 1900043.
- 9 X. Peng and H. Wang, *J. Polym. Sci., Part B: Polym. Phys.*, 2018, **56**, 1314–1324.
- 10 J. Shang, X. Le, J. Zhang, T. Chen and P. Theato, *Polym. Chem.*, 2019, **10**, 1036–1055.

- 11 Y. Liu, J. K. Boyles, J. Genzer and M. D. Dickey, *Soft Matter*, 2012, **8**, 1764–1769.
- 12 M. D. Hager, S. Bode, C. Weber and U. S. Schubert, *Prog. Polym. Sci.*, 2015, **49–50**, 3–33.
- 13 Q. Zhao, H. J. Qi and T. Xie, *Prog. Polym. Sci.*, 2015, **49–50**, 79–120.
- 14 S.-k. Ahn and R. M. Kasi, *Adv. Funct. Mater.*, 2011, **21**, 4543–4549.
- 15 T. J. White and D. J. Broer, *Nat. Mater.*, 2015, **14**, 1087–1098.
- 16 C. Ohm, M. Brehmer and R. Zentel, *Adv. Mater.*, 2010, **22**, 3366–3387.
- 17 H. Shahsavan, L. Yu, A. Jákli and B. Zhao, *Soft Matter*, 2017, **13**, 8006–8022.
- 18 Y. Shang, J. Wang, T. Ikeda and L. Jiang, *J. Mater. Chem. C*, 2019, **7**, 3413–3428.
- 19 L. T. de Haan, A. P. H. J. Schenning and D. J. Broer, *Polymer*, 2014, **55**, 5885–5896.
- 20 H. Jiang, C. Li and X. Huang, *Nanoscale*, 2013, **5**, 5225–5240.
- 21 S.-J. Jeon, A. W. Hauser and R. C. Hayward, *Acc. Chem. Res.*, 2017, **50**, 161–169.
- 22 T. Mu, L. Liu, X. Lan, Y. Liu and J. Leng, *Compos. Sci. Technol.*, 2018, **160**, 169–198.
- 23 V. Cresta, G. Romano, A. Kolpak, B. Zalar and V. Domenici, *Polymers*, 2018, **10**, 773.
- 24 R. S. Kularatne, H. Kim, J. M. Boothby and T. H. Ware, *J. Polym. Sci., Part B: Polym. Phys.*, 2017, **55**, 395–411.
- 25 A. Priimagi, C. J. Barrett and A. Shishido, *J. Mater. Chem. C*, 2014, **2**, 7155–7162.
- 26 B. A. Kowalski, T. C. Guin, A. D. Augustine, N. P. Godman and T. J. White, *ACS Macro Lett.*, 2017, **6**, 436–441.
- 27 M. E. McConney, A. Martinez, V. P. Tondiglia, K. M. Lee, D. Langley, I. I. Smalyukh and T. J. White, *Adv. Mater.*, 2013, **25**, 5880–5885.
- 28 T. H. Ware, M. E. McConney, J. J. Wie, V. P. Tondiglia and T. J. White, *Science*, 2015, **347**, 982–984.
- 29 S.-k. Ahn, T. H. Ware, K. M. Lee, V. P. Tondiglia and T. J. White, *Adv. Funct. Mater.*, 2016, **26**, 5819–5826.
- 30 B. R. Donovan, V. M. Matavulj, S.-K. Ahn, T. Guin and T. J. White, *Adv. Mater.*, 2019, **31**, 1805750.
- 31 D. Liu and D. J. Broer, *Langmuir*, 2014, **30**, 13499–13509.
- 32 J. Cui, D.-M. Drotlef, I. Larrazza, J. P. Fernández-Blázquez, L. F. Boesel, C. Ohm, M. Mezger, R. Zentel and A. del Campo, *Adv. Mater.*, 2012, **24**, 4601–4604.
- 33 A. Buguin, M.-H. Li, P. Silberzan, B. Ladoux and P. Keller, *J. Am. Chem. Soc.*, 2006, **128**, 1088–1089.
- 34 H. Yang, A. Buguin, J.-M. Taulemesse, K. Kaneko, S. Méry, A. Bergeret and P. Keller, *J. Am. Chem. Soc.*, 2009, **131**, 15000–15004.
- 35 H. Zhao, J. J. Wie, D. Copic, C. R. Oliver, A. Orbaek White, S. Kim and A. J. Hart, *ACS Appl. Mater. Interfaces*, 2016, **8**, 8110–8117.
- 36 S. Schuhladden, F. Preller, R. Rix, S. Petsch, R. Zentel and H. Zappe, *Adv. Mater.*, 2014, **26**, 7247–7251.
- 37 S. Petsch, B. Khatir, S. Schuhladden, L. Köbele, R. Rix, R. Zentel and H. Zappe, *Smart Mater. Struct.*, 2016, **25**, 085010.
- 38 C. Ambulo, J. J. Burroughs, J. M. Boothby, H. Kim, M. R. Shankar and T. H. Ware, *ACS Appl. Mater. Interfaces*, 2017, **9**, 37332–37339.
- 39 M. O. Saed, C. P. Ambulo, H. Kim, R. De, V. Raval, K. Searles, D. A. Siddiqui, J. M. O. Cue, M. C. Stefan, M. R. Shankar and T. H. Ware, *Adv. Funct. Mater.*, 2019, **29**, 1806412.
- 40 M. López-Valdeolivas, D. Liu, D. J. Broer and C. Sánchez-Somolinos, *Macromol. Rapid Commun.*, 2018, **39**, 1700710.
- 41 A. Kotikian, R. L. Truby, J. W. Boley, T. J. White and J. A. Lewis, *Adv. Mater.*, 2018, **30**, 1706164.
- 42 D. J. Roach, X. Kuang, C. Yuan, K. Chen and H. J. Qi, *Smart Mater. Struct.*, 2018, **27**, 125011.
- 43 J. K  pfer and H. Finkelmann, *Macromol. Rapid Commun.*, 1991, **12**, 717–726.
- 44 H. Wermter and H. Finkelmann, *e-Polymers*, 2001, **1**, 111.
- 45 A. Komp and H. Finkelmann, *Macromol. Rapid Commun.*, 2007, **28**, 55–62.
- 46 B. Donnio, H. Wermter and H. Finkelmann, *Macromolecules*, 2000, **33**, 7724–7729.
- 47 D. Rogez, S. Krause and P. Martinoty, *Soft Matter*, 2018, **14**, 6449–6462.
- 48 H. Finkelmann, E. Nishikawa, G. G. Pereira and M. Warner, *Phys. Rev. Lett.*, 2001, **87**, 015501.
- 49 A. Sanchez-Ferrer and H. Finkelmann, *Soft Matter*, 2013, **9**, 4621–4627.
- 50 J. Garcia-Amor  s, H. Finkelmann and D. Velasco, *J. Mater. Chem.*, 2011, **21**, 1094–1101.
- 51 M. Camacho-Lopez, H. Finkelmann, P. Palfy-Muhoray and M. Shelley, *Nat. Mater.*, 2004, **3**, 307–310.
- 52 M. Chambers, H. Finkelmann, M. Remskar, A. Sanchez-Ferrer, B. Zalar and S. Zumer, *J. Mater. Chem.*, 2009, **19**, 1524–1531.
- 53 M. Wang, S. M. Sayed, L.-X. Guo, B.-P. Lin, X.-Q. Zhang, Y. Sun and H. Yang, *Macromolecules*, 2016, **49**, 663–671.
- 54 A. Agrawal, H. Chen, H. Kim, B. Zhu, O. Adetiba, A. Miranda, A. Cristian Chipara, P. M. Ajayan, J. G. Jacot and R. Verduzco, *ACS Macro Lett.*, 2016, **5**, 1386–1390.
- 55 C. M. Yakacki, M. Saed, D. P. Nair, T. Gong, S. M. Reed and C. N. Bowman, *RSC Adv.*, 2015, **5**, 18997–19001.
- 56 M. O. Saed, A. H. Torbati, C. A. Starr, R. Visvanathan, N. A. Clark and C. M. Yakacki, *J. Polym. Sci., Part B: Polym. Phys.*, 2017, **55**, 157–168.
- 57 C. Ahn, X. Liang and S. Cai, *Extreme Mech. Lett.*, 2015, **5**, 30–36.
- 58 Y. Li, S. Hamed, R. Geoffrey, Z. Che, S. Pengxiang and Z. Boxin, *Adv. Funct. Mater.*, 2018, 1802809.
- 59 M. Barnes and R. Verduzco, *Soft Matter*, 2019, **15**, 870–879.
- 60 Z. Wang, H. Tian, Q. He and S. Cai, *ACS Appl. Mater. Interfaces*, 2017, **9**, 33119–33128.
- 61 Z. Wang, Q. He, Y. Wang and S. Cai, *Soft Matter*, 2019, **15**, 2811–2816.
- 62 A. L. Hagstrom, H.-L. Lee, M.-S. Lee, H.-S. Choe, J. Jung, B.-G. Park, W.-S. Han, J.-S. Ko, J.-H. Kim and J.-H. Kim, *ACS Appl. Mater. Interfaces*, 2018, **10**, 8985–8992.
- 63 T. H. Ware and T. J. White, *Polym. Chem.*, 2015, **6**, 4835–4844.
- 64 H.-H. Yoon, D.-Y. Kim, K.-U. Jeong and S.-K. Ahn, *Macromolecules*, 2018, **51**, 1141–1149.
- 65 A. Rigail-Cede  o and C. S. P. Sung, *Polymer*, 2005, **46**, 9378–9384.

- 66 K. M. Lee, H. Koerner, R. A. Vaia, T. J. Bunning and T. J. White, *Macromolecules*, 2010, **43**, 8185–8190.
- 67 T. H. Ware, J. S. Biggins, A. F. Shick, M. Warner and T. J. White, *Nat. Commun.*, 2016, **7**, 10781.
- 68 J. J. Wie, K. M. Lee, M. L. Smith, R. A. Vaia and T. J. White, *Soft Matter*, 2013, **9**, 9303–9310.
- 69 K. M. Lee, T. J. Bunning and T. J. White, *Adv. Mater.*, 2012, **24**, 2839–2843.
- 70 L. T. de Haan, C. Sánchez-Somolinos, C. M. W. Bastiaansen, A. P. H. J. Schenning and D. J. Broer, *Angew. Chem., Int. Ed.*, 2012, **51**, 12469–12472.
- 71 O. M. Wani, H. Zeng, P. Wasylczyk and A. Priimagi, *Adv. Opt. Mater.*, 2018, **6**, 1700949.
- 72 Y. Xia, G. Cedillo-Servin, R. D. Kamien and S. Yang, *Adv. Mater.*, 2016, **28**, 9637–9643.
- 73 N. Torras, K. E. Zinoviev, J. Esteve and A. Sanchez-Ferrer, *J. Mater. Chem. C*, 2013, **1**, 5183–5190.
- 74 D. J. Roach, C. Yuan, X. Kuang, V. C.-F. Li, P. Blake, M. L. Romero, I. Hammel, K. Yu and H. J. Qi, *ACS Appl. Mater. Interfaces*, 2019, **11**, 19514–19521.
- 75 J. Naciri, A. Srinivasan, H. Jeon, N. Nikolov, P. Keller and B. R. Ratna, *Macromolecules*, 2003, **36**, 8499–8505.
- 76 E.-K. Fleischmann, F. R. Forst and R. Zentel, *Macromol. Chem. Phys.*, 2014, **215**, 1004–1011.
- 77 A. H. Gelebart, M. Mc Bride, A. P. H. J. Schenning, C. N. Bowman and D. J. Broer, *Adv. Funct. Mater.*, 2016, **26**, 5322–5327.
- 78 J. M. Boothby, H. Kim and T. H. Ware, *Sens. Actuators, B*, 2017, **240**, 511–518.
- 79 T. Kamal and S.-Y. Park, *Chem. Commun.*, 2014, **50**, 2030–2033.
- 80 T. Kamal and S.-Y. Park, *ACS Appl. Mater. Interfaces*, 2014, **6**, 18048–18054.
- 81 X. Liu, R. Wei, P. T. Hoang, X. Wang, T. Liu and P. Keller, *Adv. Funct. Mater.*, 2015, **25**, 3022–3032.
- 82 S. A. Turner, J. Zhou, S. S. Sheiko and V. S. Ashby, *ACS Appl. Mater. Interfaces*, 2014, **6**, 8017–8021.
- 83 Z. L. Wu, A. Buguin, H. Yang, J.-M. Taulemesse, N. Le Moigne, A. Bergeret, X. Wang and P. Keller, *Adv. Funct. Mater.*, 2013, **23**, 3070–3076.
- 84 Y. Zhan, J. Zhao, W. Liu, B. Yang, J. Wei and Y. Yu, *ACS Appl. Mater. Interfaces*, 2015, **7**, 25522–25528.
- 85 W. Feng, D. J. Broer and D. Liu, *Adv. Mater.*, 2018, **30**, 1704970.
- 86 D. Liu and D. J. Broer, *Angew. Chem., Int. Ed.*, 2014, **53**, 4542–4546.
- 87 C. Li, Y. Zhang, J. Ju, F. Cheng, M. Liu, L. Jiang and Y. Yu, *Adv. Funct. Mater.*, 2012, **22**, 760–763.